


Native topological readout on qubit hardware: a Fibonacci-chain benchmark of measurement-compilation trade-offs

Babatunde Moses Ayeni ^{1,2}

¹*Department of Physics, Maynooth University*

²*School of Mathematics and Statistics, Technological University Dublin*

(Dated: May 26, 2026)

Recent demonstrations of non-Abelian braiding of graph vertices on noisy intermediate-scale quantum (NISQ) superconducting processor, and the experimental realization of topological order in general on various quantum hardware platforms necessitate an important question: when does a native (topological) fusion readout genuinely help for topological anyonic Hamiltonians implemented on NISQ hardware? We use the Fibonacci anyons chain as a concrete model for understanding the trade-off between measurement cost and compilation cost in that setting. The comparison is made against a simple grouped-Pauli baseline, and is scored by a covariance-aware mean-squared-error (MSE) of the full energy estimator. We based our benchmark on two different important classes of quantum circuits, namely Floquet time-evolved and variational quantum eigensolver quantum circuits, with the underlying Hamiltonian consisting of both braiding and fusion interaction. Our analysis found that there is not a uniform best method across both problems: the fusion readout method performed better on Floquet-type circuits on both the MSE and covariance-aware sampling variance, while the grouped Pauli method performed better on VQE on the MSE but worse on sampling variance. We derive scaling laws, and compute shot-budget crossover points, where one method is operationally favored above the other. The relevance of this work extends beyond Fibonacci chains to two-dimensional topological models compiled on superconducting and other qubit-native platforms, and can be used as a guide in answering the question of when one should measure in the native operator basis of the target physics, or when it is better to fall back on Pauli-basis reconstruction.

I. INTRODUCTION

Near-term quantum algorithms are constrained not only by coherent gate error but also by measurement cost: the number of circuits, shot pools, and classical post-processing steps required to estimate observables to useful precision [1–3]. This becomes particularly severe when a target Hamiltonian is hosted on qubit hardware but its physically natural observables are not short Pauli sums in the device basis. An important class of such Hamiltonians are topological models with non-Abelian anyonic excitations. Operationally, the issue is simple: a qubit processor only returns qubit readout data, so an encoded topological observable must be accessed either by reconstructing it from Pauli-basis measurements or by compiling an extra unitary that rotates the state into a basis where ordinary qubit readout implements the desired projector or fusion measurement. A large literature has therefore focused on making Pauli-frame estimation more efficient through commuting-group strategies, adaptive allocation, low-rank factorizations, and shadow-like methods [4–11]. Recent refinements also include exhaustive searches for larger commuting measurement groupings within VQE-style estimators [12]. Those advances sharpen the question that matters for structured models: when should one remain in the Pauli frame and optimize within it, and when is it better to leave that frame and pay additional compilation cost to measure in a basis adapted to the target physics?

We use the Fibonacci anyons chain with both topological braiding and fusion interaction as a sort of minimal

model to study this problem. That question is broader than the Fibonacci chain alone. It arises whenever topological or projector-dominated models are compiled onto qubit-native processors: in anyonic topological engineering on superconducting hardware, in string-net or Levin-Wen-type Hamiltonians represented on superconducting quantum processors, and in code-space or defect-based braiding architectures, the target observables are often most natural in fusion, projector, or constraint variables rather than in the bare Pauli language of the host device [13–20]. Recent processor-level demonstrations now make that broader motivation more concrete, including non-Abelian braiding of graph vertices on superconducting hardware, trapped-ion demonstrations of non-Abelian topological order, and superconducting realizations targeted specifically at Fibonacci anyons. [21–23] Once such models are hosted on qubit hardware, one still faces a measurement-design choice: reconstruct the observable in the Pauli frame of the processor, or compile a measurement into the native operator basis of the encoded topological model.

Fibonacci anyon chains provide a natural flagship setting for studying that trade-off. Their local observables are fusion-channel projectors, and the corresponding native basis changes are written directly in terms of the same F - and R -matrices primitives that define the theory [24–30]. This is why fusion readout is more than an arbitrary alternative measurement prescription: it is a readout strategy aligned with the observable structure of the Hamiltonian itself.

It is important to state that we model Fibonacci

anyons on quantum hardware through an encoding of the fusion space, and not through a direct engineering of anyonic excitations, as in some recent experimental papers.[21–23] Still the question we asked remains relevant once topological models are compiled onto non-native quantum processors (e.g. superconducting): if the target observable is native in the encoded anyonic description, should it still be measured through Pauli reconstruction, or should one pay the extra basis-change depth required to measure it more natively? ¹

We organize our benchmark around a covariance-aware fixed-budget MSE of the full energy estimator, and not around covariance in isolation. The reference baseline chosen is the grouped Pauli sampling with qubit-wise-commuting groups (PS_{QWC}), because it is transparent and interpretable rather than because it is the strongest possible generic Pauli estimator. The aim of this work is not to find a single winner in the measurement-optimization problem, but to test whether a measurement rule that is physically aligned with a topological Hamiltonian can retain its estimator-level advantage after compilation to a constrained NISQ backend.

The paper makes four concrete points. First, it formulates the estimator-level criterion that tests whether a native measurement advantage survives at fixed shot budget. Second, it benchmarks the fusion readout (FR) against the qubit-wise grouped Pauli strategy (PS_{QWC}) on a digital Floquet-type evolution, and on optimized VQE shallow circuits of Fibonacci-chain Hamiltonians. Third, it shows that noiseless and hardware comparisons need not agree: FR wins uniformly on covariance-aware sampling variance, but not uniformly on realized estimator error. Fourth, it connects that crossover to a resource-proxy analysis derived from the same scaling-law fits used in the main results. The upshot of our analysis can be stated simply as, native fusion readout provides a real sampling advantage, but compiled hardware cost can still determine the practical winner under NISQ constraints. Even if this could have been surmised intuitively, our work demonstrates this rigorously both qualitatively and quantitatively.

The rest of this article is organized as follows. Section II defines the Fibonacci-chain Hamiltonian and explains why fusion readout is native to its local observables. Section III develops the covariance-aware fixed-budget estimator framework and states the criterion used to compare FR with grouped Pauli reconstruction. Section IV specifies the two measurement strategies, the digital Floquet and optimized-state VQE workloads, and the matched-budget hardware protocol. Section V presents the noiseless and hardware results, Section VI discusses

their implications for compiled topological measurements on NISQ hardware, and Section VII concludes. The appendices collect the Fibonacci F/R conventions, selected crossover-scaling grids, the resource-proxy scaling analysis, and the hardware transpilation methodology.

II. FIBONACCI ANYONS CHAIN MODEL AND NATIVE OBSERVABLES

We consider one-dimensional Fibonacci anyon chains in the fusion-path encoding [27–31]. In this encoding, each qubit stores an intermediate fusion label, with $|0\rangle \leftrightarrow \mathbf{1}$ and $|1\rangle \leftrightarrow \tau$, and only fusion-consistent bit strings represent physical states. The local observables are short-range projector-type terms, making the model a natural setting for comparing Pauli-frame estimation with a native anyonic readout.

The Hamiltonian studied throughout this work consists of neighbouring and next-neighbouring interactions, which can be written as

$$H_n = J_{F3} \sum_{i=0}^{n-3} H_i^{F3} + J_{BF4} \sum_{i=0}^{n-4} H_i^{BF4}, \quad (1)$$

with local terms

$$H_i^{F3} = F_i^\dagger Z_{i+1} F_i, \quad (2)$$

$$H_i^{BF4} = B_i^\dagger F_{i+1}^\dagger Z_{i+2} F_{i+1} B_i, \quad (3)$$

where H_i^{F3} is the (τ_i, τ_{i+1}) neighbouring interaction term that maps to three qubits and H_i^{BF4} is the $(\tau_i, \cdot, \tau_{i+2})$ next-neighbouring interaction term that maps to four qubits, as shown below. Here F_i is the local recoupling move on the (fusion tree) window $(i, i+1, i+2)$ and B_i is the braid operator in the same fusion-tree language, where B_i might be composed of the F- and R-matrices as appropriate. Throughout our benchmark we fix the values of the coefficients as $J_{F3} = 1.0$ and $J_{BF4} = 0.5$. Appendix A records the explicit Fibonacci F, R , and B conventions and the implementation-level braid identity used by the compiled circuits. Therefore, in the fusion-path encoding, the entire Hamiltonian of n anyons maps onto $n + 1$ qubits.

The structural reason that fusion readout is native can be seen easily by considering the BF4 term: H_i^{BF4} , which represents the interaction between τ_i and τ_{i+2} . To foster this interaction, both anyons have to be brought into neighbouring positions using a braid move B_i . Let h_{i+1}^{DF} now be the local (projector-type) observable acting on the two neighbouring anyons (τ_{i+1}, τ_{i+2}) in a direct fusion. The physical interaction may be completely written as

$$H_i^{BF4} = B_i^\dagger F_{i+1}^\dagger h_{i+1}^{DF} F_{i+1} B_i. \quad (4)$$

The details are contained in the Appendix. For an arbitrary prepared state ρ , the corresponding local expecta-

¹ One can think of the encoded problem as the mathematical model of the physical anyons topological engineering problem. So, the measurement-compilation cost tradeoff in the physical problem should similarly manifest in the simulation of its mathematical model.

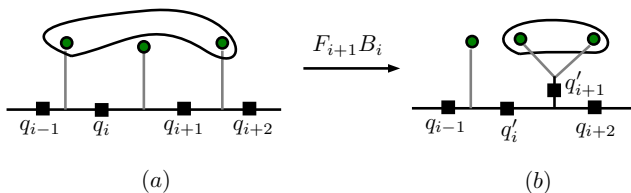


FIG. 1. Native-measurement motivation for the Fibonacci-chain Hamiltonian. The local basis change $U_i = F_{i+1}B_i$ maps the BF4 interaction into a direct-fusion frame where the corresponding observable is a simple local projector. Fusion read-out is therefore aligned with the observable structure of the model rather than introduced as an arbitrary competitor in a generic measurement comparison.

tion value admits two equivalent trace forms

$$\langle H_i^{\text{BF4}} \rangle_\rho = \text{Tr} \left(B_i^\dagger F_{i+1}^\dagger h_{i+1}^{\text{DF}} F_{i+1} B_i \rho \right) \quad (5)$$

$$\equiv \text{Tr} \left(h_{i+1}^{\text{DF}} F_{i+1} B_i \rho B_i^\dagger F_{i+1}^\dagger \right). \quad (6)$$

Equation (5) and (6) already contains the two measurement logics used in the paper. In PS_{QWC}, one measures a grouped Pauli decomposition of the mapped operator content on the state in Eq. (5). In FR, one instead appends the basis change $U_i = F_{i+1}B_i$ to the state-preparation circuit and measures the direct-fusion observable h_{i+1}^{DF} directly on the rotated state as in Eq. (6). The same logic extends termwise to the full Hamiltonian in Eq. (1). Even though both methods are equivalent in principle, in practice they behave differently on NISQ processor, where they have different compilation and measurement-error cost.

The next section turns this structural observation into an estimator-level comparison framework. It defines the fixed-budget energy estimator, separates covariance-driven sampling effects from hardware-sensitive contributions, and derives the crossover criterion used to decide when the native sampling advantage of FR survives compiled execution.

III. ESTIMATOR FRAMEWORK AND NATIVE-MEASUREMENT CRITERION

For the purposes of the benchmark, the Hamiltonian is written abstractly as

$$H = \sum_{\ell=1}^L w_\ell O_\ell, \quad (7)$$

where the O_ℓ are fixed local observables and w_ℓ the corresponding weights, which we write as a vector $\mathbf{w} = (w_1, \dots, w_L)^\text{T}$. For each method $m \in \{\text{FR}, \text{PS}_{\text{QWC}}\}$ and total shot budget N , the full-Hamiltonian estimator is

$$\hat{E}_m^{(N)} = \sum_{\ell=1}^L w_\ell \hat{o}_{\ell,m}^{(N)} = \mathbf{w}^\text{T} \hat{\mathbf{o}}_m^{(N)}, \quad (8)$$

where $\hat{\mathbf{o}}_m^{(N)}$ is a vector of the estimators of each fixed local observable O_ℓ .

The benchmark quantity is the fixed-budget mean-squared error

$$\text{MSE}_m(N) = \mathbb{E} \left[\left(\hat{E}_m^{(N)} - E_{\text{exact}} \right)^2 \right]. \quad (9)$$

Writing the mean estimator value as

$$\mu_m(N) = \mathbb{E} \left[\hat{E}_m^{(N)} \right], \quad (10)$$

and the bias term as

$$b_m(N) = \mu_m(N) - E_{\text{exact}}, \quad (11)$$

the standard add-and-subtract step gives

$$\text{MSE}_m(N) = b_m(N)^2 + \text{Var} \left(\hat{E}_m^{(N)} \right). \quad (12)$$

This is the quantity we used to benchmark the cost of doing measurement in the native FR method against the simple PS_{QWC} method.

To isolate sampling variance from hardware noise, we split the estimator variance as

$$\text{Var} \left(\hat{E}_m^{(N)} \right) = \text{Var}_{\text{sample},m}(N) + \text{Var}_{\text{hw},m}(N), \quad (13)$$

where the covariance-aware sampling term is

$$\text{Var}_{\text{sample},m}(N) = \mathbf{w}^\text{T} \Sigma_m(N) \mathbf{w}, \quad (14)$$

$$\Sigma_m(N) = \text{Cov} \left(\hat{\mathbf{o}}_m^{(N)} \right), \quad (15)$$

and $\text{Var}_{\text{hw},m}(N)$ is the variance term due to hardware noise. At fixed circuit family and fixed shot-allocation fractions we write the large- N form as

$$\Sigma_m(N) = \frac{\tilde{\Sigma}_m}{N} + o(N^{-1}), \quad \Gamma_m = \mathbf{w}^\text{T} \tilde{\Sigma}_m \mathbf{w}, \quad (16)$$

so that the leading sampling variance contribution is Γ_m/N .

This motivates the leading-order model

$$\text{MSE}_m(N) \approx b_m(N)^2 + \frac{\Gamma_m + \kappa_m}{N}, \quad (17)$$

where κ_m absorbs the hardware-sensitive $1/N$ contribution. The difference between methods is therefore controlled by

$$\Delta_{\text{MSE}}(N) = \text{MSE}_{\text{FR}}(N) - \text{MSE}_{\text{PS}_{\text{QWC}}}(N) \quad (18)$$

$$\approx \Delta b^2 + \frac{\Delta \Gamma_{\text{eff}}}{N}, \quad (19)$$

with $\Delta b^2 = b_{\text{FR}}^2 - b_{\text{PS}_{\text{QWC}}}^2$ and $\Delta \Gamma_{\text{eff}} = (\Gamma_{\text{FR}} + \kappa_{\text{FR}}) - (\Gamma_{\text{PS}_{\text{QWC}}} + \kappa_{\text{PS}_{\text{QWC}}})$. The crossover point (where $\Delta_{\text{MSE}}(N) = 0$) is obtained as $N_c \approx -\Delta \Gamma_{\text{eff}} / \Delta b^2$. If we make the reasonable assumptive choice that $\Delta \Gamma_{\text{eff}} < 0$

and $\Delta b^2 > 0$, as supported empirically by data below, then the characteristic crossover scale is

$$N_c \approx \frac{|\Delta\Gamma_{\text{eff}}|}{\Delta b^2}. \quad (20)$$

This is the central criterion of the paper: native fusion readout is useful only when its covariance advantage survives the non-sampling penalty introduced by compiled hardware execution.

IV. MEASUREMENT STRATEGIES AND BENCHMARK WORKLOADS

In this section we describe the measurement strategies and the quantum problems. We first specify how FR and PS_{QWC} estimate the same local Hamiltonian terms, then define the two quantum circuit families used throughout the comparison: digital Floquet-evolved states and optimized-state VQE circuits. We close by stating the matched shot-budget rule and the hardware-execution protocol that put both measurement strategies on the same footing.

A. Fusion readout and grouped Pauli reconstruction

For fusion readout, each local term is measured in a problem-adapted native frame. Concretely, for each observable O_ℓ we compile a short basis change U_ℓ such that

$$O_\ell = U_\ell^\dagger h_\ell^{\text{native}} U_\ell, \quad (21)$$

with h_ℓ^{native} diagonal or otherwise low support in the encoded qubit basis. The local estimator is then

$$o_\ell = \text{Tr}(\rho O_\ell) = \text{Tr}\left(U_\ell \rho U_\ell^\dagger h_\ell^{\text{native}}\right), \quad (22)$$

$$\hat{o}_{\ell,\text{FR}}^{(r)} = \frac{1}{N_{\ell,r}} \sum_{s=1}^{N_{\ell,r}} x_{\ell,s}^{(r)}, \quad x_{\ell,s}^{(r)} \in \text{spec}(h_\ell^{\text{native}}), \quad (23)$$

where r labels replicates. For the Fibonacci-chain Hamiltonian, the number of native measurement circuits is one per local term, hence $2n - 5$ circuits at qubit number n .

For PS_{QWC}, the same local observable is reconstructed from a grouped Pauli expansion,

$$O_\ell = \sum_{\alpha=1}^M a_{\ell\alpha} P_\alpha, \quad \{1, \dots, M\} = \bigsqcup_{g=1}^G \mathcal{G}_g, \quad (24)$$

$$\hat{o}_{\ell,\text{PSQWC}}^{(r)} = \sum_{\alpha=1}^M a_{\ell\alpha} \hat{p}_\alpha^{(r)}, \quad (25)$$

where each group \mathcal{G}_g is qubit-wise commuting and the reconstructed Pauli expectations $\hat{p}_\alpha^{(r)}$ are extracted from the shared group counts.

The hierarchy of sampled objects matters. One shot is one execution of one measurement circuit. One replicate is one full rerun of the complete estimator at fixed total budget N , including all method-specific sub-allocations. The estimator is therefore fundamentally defined over shots, while replicates are used only to estimate fixed-budget moments of that estimator empirically.

Collecting the local estimators into $\hat{o}_m^{(r)}$ for replicate r , the Hamiltonian-energy estimate and the covariance-aware sampling-variance estimator are

$$\hat{E}_m^{(r)} = \mathbf{w}^\top \hat{o}_m^{(r)}, \quad \hat{\text{Var}}_m^{(r)} = \mathbf{w}^\top \Sigma_m^{(r)} \mathbf{w}. \quad (26)$$

Across R replicates, the empirical fixed-budget estimators for the energy and MSE are

$$\bar{E}_m = \frac{1}{R} \sum_{r=1}^R \hat{E}_m^{(r)}, \quad (27)$$

$$\widehat{\text{MSE}}_m^{\text{emp}} = \frac{1}{R} \sum_{r=1}^R \left(\hat{E}_m^{(r)} - E_{\text{exact}} \right)^2. \quad (28)$$

For the empirical MSE itself, we quantify the within-cell uncertainty by the replicate standard error of the squared errors,

$$\widehat{\text{SE}}_{\text{MSE},m} = \frac{s_{\text{sq},m}}{\sqrt{R}},$$

$$s_{\text{sq},m}^2 = \frac{1}{R-1} \sum_{r=1}^R \left[\left(\hat{E}_m^{(r)} - E_{\text{exact}} \right)^2 - \widehat{\text{MSE}}_m^{\text{emp}} \right]^2, \quad (29)$$

and use the corresponding pooled FR-versus-PS standard error below as a descriptive uncertainty proxy for cellwise empirical-MSE differences.

B. Digital Floquet evolution

The digital benchmark uses a Floquet-type time evolution to generate states that can be used as a controlled family of comparison data without a classical optimizer feedback.

With the Hamiltonian from Eq. (1), the logical product-formula circuit is

$$V(s) = \left(\prod_j e^{-i \delta t H_j} \right)^s, \quad \rho_n(s) = V(s) \rho_0 V^\dagger(s), \quad (30)$$

where s is the Trotter-step count and $\rho_0 = |1 \dots 1\rangle\langle 1 \dots 1|$ is the fixed fusion-valid reference state used throughout the benchmark. One step is built from ordered sweeps over the F3 and BF4 terms,

$$U_A = \prod_{j=0}^{n-3} \left(U_F^{(j)} e^{-i \delta t J_{\text{F3}} Z_{j+1}} U_F^{(j)\dagger} \right), \quad (31)$$

$$U_B = \prod_{j=0}^{n-4} \left(U_{\text{BF}}^{(j)} e^{-i \delta t J_{\text{BF4}} Z_{j+2}} U_{\text{BF}}^{(j)\dagger} \right), \quad (32)$$

with $U_{\text{BF}}^{(j)} = U_F^{(j+1)}U_B^{(j)}$, so that $V(1) = U_B U_A$ and $V(s) = (V(1))^s$. Here $U_F^{(j)}$ is the local three-anyon recoupling unitary gate on window $(j, j+1, j+2)$, while $U_B^{(j)}$ is the corresponding braid unitary gate. Both are summarized in Appendix A.

The digital observable is the total Hamiltonian energy

$$E_{\text{dig}}(n, s) = \text{Tr}[\rho_n(s)H_n]. \quad (33)$$

The noiseless simulations and (noisy) quantum-hardware experiments cover $n = 5, 7, 9, 11$ qubits and Trotter steps $s = 1, \dots, 6$, for a total shot-budget range $N \in \{2000, 4000, 8000, 16000\}$.

C. Optimized-state VQE circuit

The second benchmarking system we used is a quantum state whose optimal circuit parameters were obtained from a VQE noiseless simulation. This help isolates measurement quality from optimizer dynamics by fixing the variational parameters before the benchmark comparison. For each system size, we first prepare an optimized “locked” reference state with a hardware-efficient next-nearest-neighbour $\text{Ry-Rz} + \text{CZ}$ ansatz and then benchmark FR and PS_{QWC} on that same state at matched shot budgets. This ansatz choice is consistent with the broader hardware-efficient VQE literature [32, 33]. Starting from the same fusion-valid reference state $|1 \cdots 1\rangle$, we write the ansatz state as

$$|\psi_n(\theta)\rangle = U_{\text{NNN}}^{(d)}(\theta) |1 \cdots 1\rangle, \quad (34)$$

with depth $d = 3$ for $n = 5, 7, 9$ and $d = 4$ for $n = 11$. A convenient explicit form is

$$U_{\text{NNN}}^{(d)}(\theta) = U_{\text{rot,f}}(\theta^{(f)}) \prod_{k=1}^d \left[U_{\text{ent}}^{(k)} U_{\text{rot}}^{(k)}(\theta^{(k)}) \right], \quad (35)$$

where

$$U_{\text{rot,f}}(\theta^{(f)}) = \prod_{j=0}^{n-1} R_z(\theta_{j,f}^{(z)}) R_y(\theta_{j,f}^{(y)}), \quad (36)$$

$$U_{\text{rot}}^{(k)}(\theta^{(k)}) = \prod_{j=0}^{n-1} R_z(\theta_{j,k}^{(z)}) R_y(\theta_{j,k}^{(y)}). \quad (37)$$

Each entangling block $U_{\text{ent}}^{(k)}$ consists of one complete nearest-neighbour CZ sweep over even and odd bonds followed by a next-nearest-neighbour sweep $\prod_{j=0}^{n-3} \text{CZ}_{j,j+2}$. For each n , a separate noiseless exact-VQE stage minimizes the Hamiltonian expectation value over this ansatz, and the resulting best parameter vector is then frozen. The quantity estimated within each comparison cell is therefore

$$E_{\text{VQE}}(n, \theta) = \langle \psi_n(\theta) | H_n | \psi_n(\theta) \rangle. \quad (38)$$

The subsequent FR-versus-PS comparison therefore probes two measurement strategies on the same locked state rather than two different optimization histories.

D. Matched shot budgets and hardware benchmark

In both workflows the two methods are compared at the same total budget N . FR partitions that budget as evenly as possible across native local observables, while PS_{QWC} partitions the same budget as evenly as possible across its global QWC groups. The hardware benchmark uses the IBM superconducting quantum processor `ibm_pittsburgh` as the compilation and execution target. No readout mitigation, dynamical decoupling, or resilience-level post-processing, and symmetry-verification-based error mitigation [34] is applied. The detailed hardware table is moved to Appendix D.

V. RESULTS: WHEN NATIVE FUSION READOUT HELPS AND WHEN IT FAILS

The results we present are generated from the datasets obtained from both noiseless simulations and quantum-hardware experiments carried out on the IBM superconducting quantum processor `ibm_pittsburgh`. In the noiseless case, each data cell uses $R = 5$ replicates, i.e. independent realizations, whereas each hardware comparison cell uses $R = 3$ replicates. The resulting hardware-side uncertainty estimates should therefore be seen as descriptive cellwise diagnostics rather than as asymptotic error bars.

We present results for the benchmark of the measurement methods executed over the workbench of digital Floquet time evolution and optimized VQE circuits.

A. Digital benchmark: realized MSE versus sampling variance

Figure 2 presents the digital benchmark in the language of the estimator criterion. The left panels show realized empirical MSE, while the right panels show the covariance-aware sampling variance from Eq. (15).

In the noiseless benchmark, FR wins 72 of 96 cells on empirical MSE and all 96 cells on mean sampling variance. This is the cleanest evidence that the native measurement alignment lowers the covariance (yielding a higher precision) and usually lowers the realized estimator error (yielding a higher accuracy) when compiled hardware noise is absent.

On the hardware benchmark, the picture becomes more nuanced. FR still wins every cell on mean sampling variance, but it wins only 71 of 96 cells on empirical MSE. That regime-level total is close to the noiseless value of 72 of 96, yet the underlying winner map is not: only 67 of 96 digital cells keep the same empirical-MSE winner between the noiseless and hardware datasets, so 29 cells reverse winner once the compiled circuits are executed on hardware. The native sampling advantage therefore survives everywhere at the covariance level, while the realized estimator ordering becomes sensitive to hardware-

induced changes in bias and empirical variance. The win count for FR is summarized in Table I.

The strongest PS-favorable tendency is concentrated in the $n = 5$ sector rather than being distributed uniformly across qubit sizes. A plausible structural contributor is that in the digital Floquet circuit, each Trotter step performs ordered left-to-right sweeps over overlapping three-qubit F3 windows and four-qubit BF4 windows associated with the nearest-neighbour and next-neighbour interaction terms. At $n = 5$ this leaves only five local terms per step, all boundary-touching, with the central qubit participating in every term, whereas the larger chains develop a genuine interior. The $n = 5$ circuit is therefore structurally exceptional, which may help explain why the PS-favorable cells concentrate there.

With the present $R = 3$ hardware realizations, many of the cellwise FR-versus-PS empirical-MSE differences are small on the scale of their own replicate-level uncertainty. Across the 96 hardware cells, the median pooled standard error for $\widehat{\Delta\text{MSE}}_{\text{emp}} = \widehat{\text{MSE}}_{\text{FR}} - \widehat{\text{MSE}}_{\text{PSQWC}}$ is 0.161, while the median absolute gap $|\widehat{\Delta\text{MSE}}_{\text{emp}}|$ is only 0.114. In other words, the typical winner margin is smaller than the uncertainty proxy attached to that margin, and only 28 of 96 cells have a gap larger than the pooled standard error. The close 71/96-versus-72/96 regime totals should therefore not be taken as evidence that the hardware and noiseless digital datasets behave identically; they reflect many weakly separated cells and a balance of cellwise reversals rather than an unchanged winner pattern.

B. Optimized-state VQE benchmark: the sharpest hardware reversal

In order not to confound the measurement benchmark test with a classical optimizer routine inherent in every VQE workflow, we first obtain the optimal ground state from a classical VQE simulation of the Hamiltonian, and then used that optimal parameters value to reconstruct the optimized circuit on either a simulator or quantum hardware before feeding it to the measurement benchmark workflow. We call such a circuit either a “locked” or optimized state.

The optimized-state VQE benchmark Figure 3 presents an entirely different view of the native-measurement method test. In the noiseless data, FR wins 15 of 16 cells on empirical MSE and all 16 cells on mean sampling variance. The native readout logic therefore behaves as expected when the comparison is not polluted by compiled hardware error.

The hardware optimized-state VQE benchmark reverses that ordering on realized error. PS_{QWC} wins 15 of 16 cells on empirical MSE, even though FR again wins all 16 cells on mean sampling variance. This is the clearest regime in the present benchmark where a genuine native sampling advantage survives at the covariance level but fails to determine the realized estimator error on hard-

TABLE I. Regime-level summary of the benchmark. The reported numbers are the total of the cells in Figure 2 where FR wins by MSE and covariance-aware sampling variance.

Benchmark	Empirical MSE	Sampling var.
Digital, noiseless	72/96	96/96
Digital, hardware	71/96	96/96
optimized-state VQE, noiseless	15/16	16/16
optimized-state VQE, hardware	1/16	16/16

ware.

This optimized-state VQE reversal is also better resolved than the mixed digital hardware pattern. With the same $R = 3$ hardware realizations, the median pooled standard error of the FR-minus-PS empirical-MSE difference across the 16 cells is 0.917, whereas the median absolute empirical-MSE gap is 1.83; 11 of 16 cells have $|\widehat{\Delta\text{MSE}}_{\text{emp}}|$ larger than that pooled error estimate. Table III also points to the likely circuit-level reason: the variational circuit is shallow, so the appended FR measurement layer remains visibly larger than the PS-QWC layer. For instance, the minimum-to-maximum total two-qubit gate counts across the set of transpiled FR versus PS-QWC circuits at the $n = 5$ qubits are 98–222 versus 51–54 respectively, and 240–370 versus 190–193 at $n = 11$ qubits. The VQE reversal on the hardware could therefore be primarily coming from the cost of appending a larger FR measurement circuit to a shallow variational circuit, whereas the PS measurement circuit is smaller.

C. Budget scaling values

Heatmap summaries are efficient description of regime structure, but the budget dependence is easier to read directly from representative cells. Figure 4 therefore shows one digital hardware cell where FR remains favored and one optimized-state VQE hardware cell where the realized-error comparison flips toward PS_{QWC}. In both panels the horizontal variable is $1/N$, the empirical-MSE values are shown as marker-only data points, and the fitted empirical-MSE trends become ordinary line models. The digital representative cell is the hardware point $(n, s) = (11, 6)$, where the highest-budget empirical difference remains negative in favor of FR. The optimized-state VQE representative cell is the $n = 7$ hardware point, where the highest-budget empirical difference is positive in favor of PS_{QWC} while the corresponding sampling-variance difference remains negative in favor of FR. These plots make the central claim concrete: the native-measurement advantage lives in the covariance-sensitive part of the estimator, but the realized hardware comparison can still be controlled by the non-sampling contribution.

Moreover, those plots reveal the scaling behaviour of the empirical MSE with the shot budget N , and its

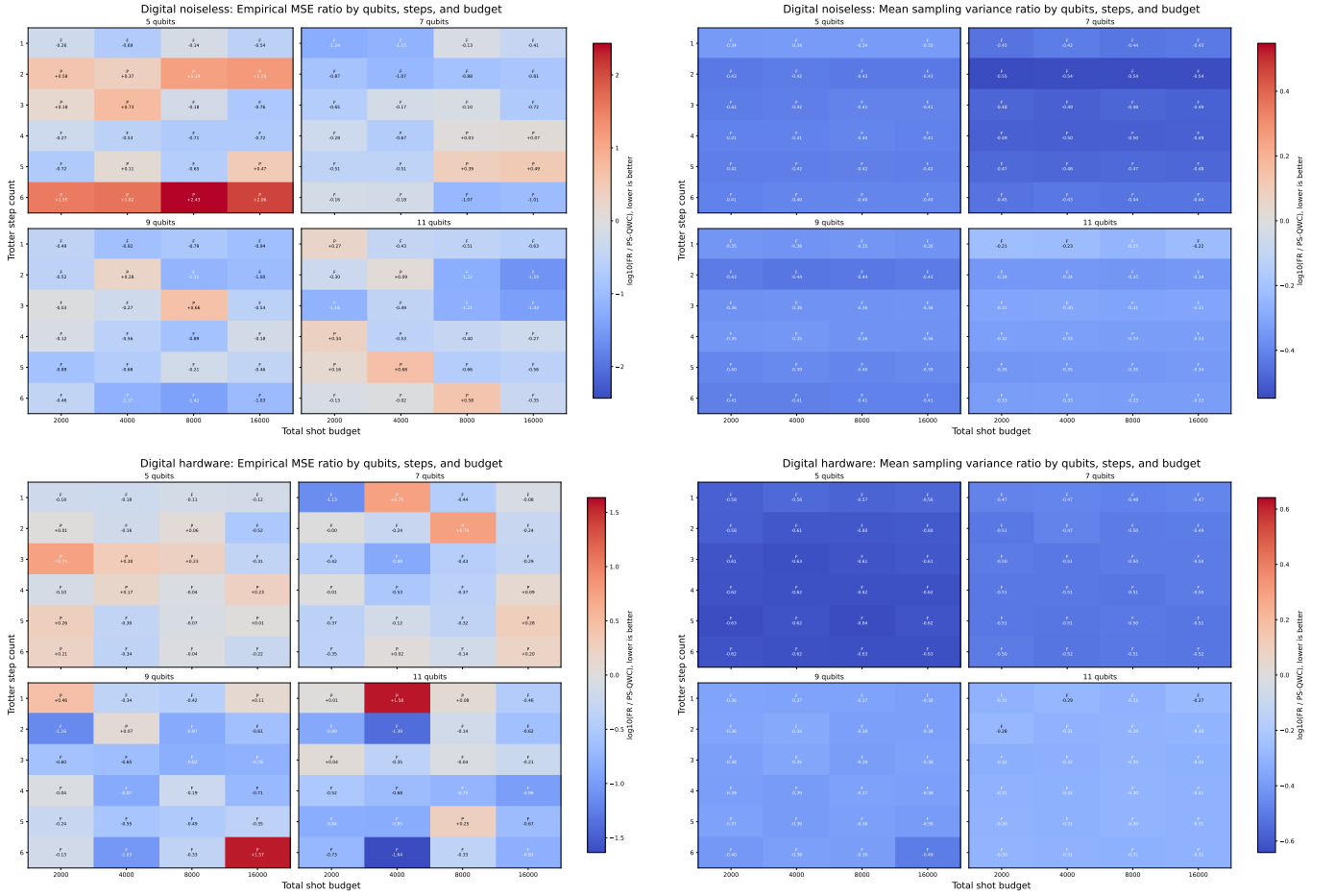


FIG. 2. Digital benchmark shown as realized estimator error versus covariance-aware sampling variance. Top row: noiseless empirical MSE and mean sampling variance. Bottom row: hardware empirical MSE and mean sampling variance. Lower values favor FR. The noiseless panels isolate the native sampling advantage; the hardware panels show where realized error partially “washes out” that advantage.

regime-dependence, which implies there might exist a crossover point between where either FR or PS_{QWC} lowers the empirical MSE. In the notation of Sec. III, the overlaid FR-solid and PS-dashed fits are interpreted as empirical realizations of $\overline{\text{MSE}}_m(N) \approx \alpha_m + \beta_m/N$, with α_m capturing the effective fixed-budget error floor and β_m capturing the covariance-sensitive slope together with hardware-sensitive $1/N$ contributions. Read this way, the digital representative cell is consistent with a favorable effective slope for FR that survives across the sampled budgets (i.e. sampling advantage), whereas the optimized-state VQE cell isolates the realized empirical-MSE reversal directly. We can use the values obtained from the empirical fits to estimate the crossover point N_c in the budget range (or outside of it), using the crossover criterion $N_c^{\text{fit}} = |\Delta\beta|/\Delta\alpha$ [as explained in Sec. III, Eq. (20)] where the FR-minus-PS fit obeys $\Delta\alpha > 0$ and $\Delta\beta < 0$ (subsequently called the “sign structure”). For the digital representative cell, the $N_c \approx 1.42 \times 10^3$, which is below the budget range considered $N \in [2000, 16000]$. For this case, PS_{QWC} favors shot budget N less than

N_c while FR favors otherwise. For the representative optimized-state VQE, the $N_c \approx 7.73 \times 10^2$, and FR favors shot budget N less than N_c while PS_{QWC} favors otherwise. This representative example shows the regime behavior of MSE for depending on the type of the physical problem being considered.

We extended this scaling analysis to the entire dataset in our work. In the digital hardware data the sign structure appears in 4 of 24 scaling cells, and all four fitted crossovers lie inside the sampled budget range $N \in [2000, 16000]$, with fitted values from 2.61×10^3 to 8.57×10^3 and median 4.53×10^3 . In the optimized-state VQE hardware data it appears in 3 of 4 scaling cells, and the median fitted value is 9.94×10^2 . The observed regime difference is therefore consistent with the same fitted criterion: in digital hardware the FR-favorable slope can still matter inside the sampled budgets, whereas in optimized-state VQE hardware the larger FR measurement circuit pushes the estimated crossover to very small budgets, making the MSE lean towards the PS-favored side of the reversal at high budgets. The crossovers are

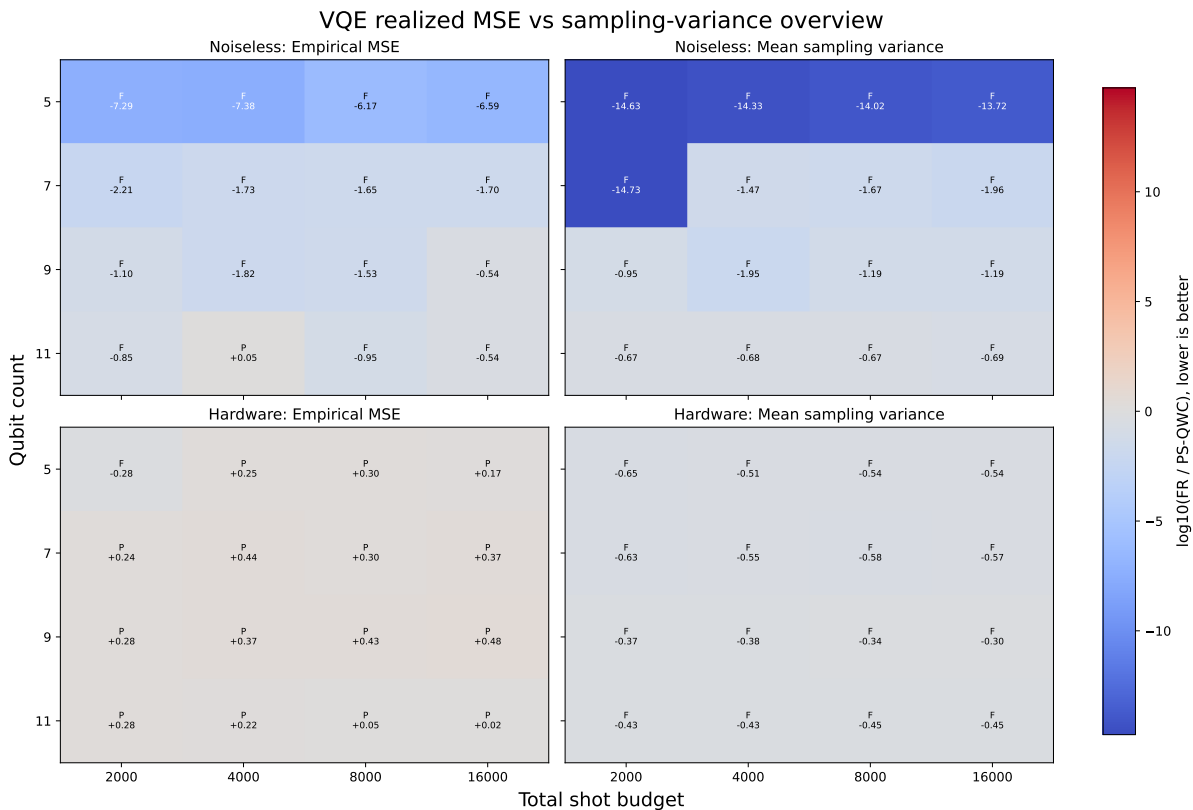


FIG. 3. Optimized-state VQE benchmark in the same realized-error-versus-sampling language used in the main text and also Figure 2. The noiseless comparison follows the native-measurement expectation, but the hardware comparison reverses on realized MSE while leaving the covariance-aware sampling advantage of FR intact.

TABLE II. Regime crossover point N_c obtained from the linear fit values for the crossover criterion Eq. 20 for both digital Floquet and optimized-VQE state on hardware.

Regime	Valid/total	Median N_c [min, max]
Digital hw	4/24	4.53×10^3 [2.61×10^3 , 8.57×10^3]
VQE hw	3/4	9.94×10^2 [7.73×10^2 , 3.52×10^3]

summarized in Table. II. These fitted crossover budgets represent descriptive thresholds in the present workload, compilation, and backend combination rather than as universal FR-versus-PS constants.

Appendix B records these fitted empirical-MSE plots of selected digital hardware cells $(n, s) \in \{5, 7, 9, 11\} \times \{1, 3, 6\}$ and the optimized-state VQE hardware cells $n = 5, 7, 9, 11$, with per-panel annotations indicating whether the fitted positive-budget crossing lies below, within, or above the sampled range.

Appendix C analyzes the correlation between the method-dependent compiled measurement layer and the common error-ratio observable $\log_{10}(\text{MSE}_{\text{FR}}/\text{MSE}_{\text{PS}})$. In the digital hardware benchmark the budget-conditioned correlation is step dependent: for the three representative panels one finds $r = +0.14$ at $s = 1$, $r = -0.45$ at $s = 3$, and $r = -0.29$ at $s = 6$. In the

locked-state VQE hardware benchmark the corresponding budget-conditioned correlation is positive, $r = +0.46$. The count-versus-error relation is therefore weak and non-universal in the digital Floquet workload, but becomes positively aligned with the PS-QWC-favorable error ratio in the shallow VQE regime.

VI. DISCUSSION

The benchmark supports a practical measurement-design statement for compiled topological models. In the Fibonacci-chain setting, fusion readout is the physically natural rule and it systematically lowers the covariance-driven sampling term. The hardware results show, however, that this advantage is not by itself a reliable predictor of realized estimator quality once the required basis changes are compiled onto a noisy qubit backend.

That is why the comparison has to be organized around fixed-budget MSE rather than covariance alone. If the question were only whether FR reduces the sampling term, the answer would be uniformly yes in the present data. The harder question is whether that benefit survives at fixed total budget after transpilation and hardware execution. Here the answer is regime dependent: the digital benchmark remains mostly favorable to FR,

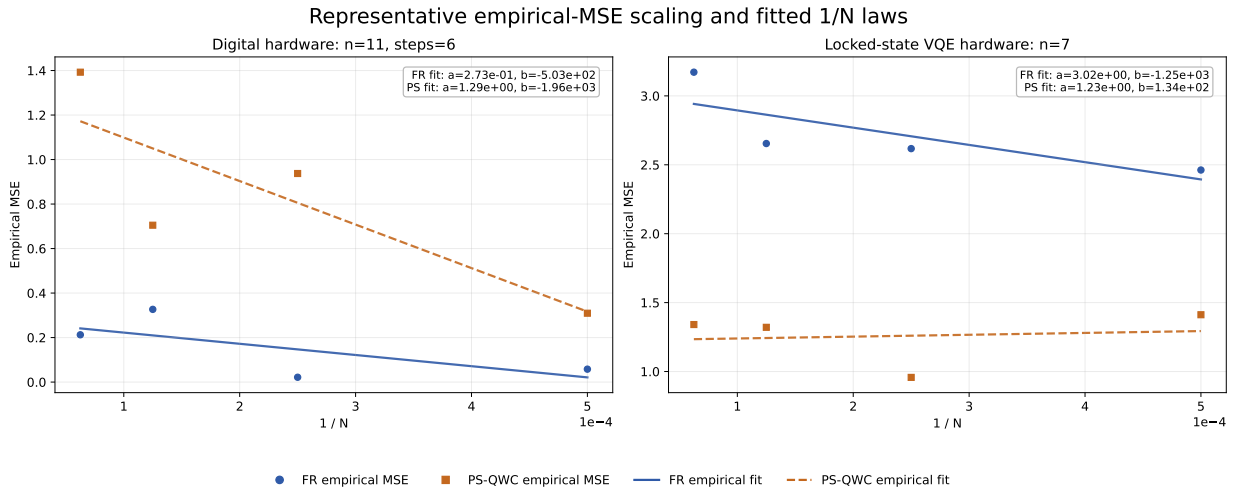


FIG. 4. Representative budget-scaling plots for one digital hardware cell and one optimized-state VQE hardware cell. Marker-only points show the empirical MSE at the sampled budgets, using circles for FR and squares for PS_{QWC}. The overlaid solid FR and dashed PS-QWC lines are least-squares fits of the form $\alpha_m + \beta_m/N$ to the empirical mean-squared-error traces. The figure makes the fitted empirical-MSE scaling visible directly in the budget traces.

while the VQE-type circuit hardware benchmark shows a clear reversal toward PS_{QWC}.

The key factor that may explain the difference between the two workbench systems is that the variational state-preparation circuit is shallow, leaving the method-dependent measurement layer relative deep: at the representative VQE endpoints of Table III, FR uses 98–222 two-qubit gates versus 51–54 for PS-QWC at $n = 5$ and 240–370 versus 190–193 at $n = 11$.² By contrast, the large digital endpoint already contains about 2.18×10^4 two-qubit gates for both methods, so the extra FR measurement layer is only a relatively small correction there. The optimized-state VQE reversal is therefore explained primarily by the larger depth of the FR measurement circuit relative to the smaller PS measurement circuit once both are appended to a shallow variational state-preparation circuit.

An important point worth noting in on the role of PS_{QWC} in the benchmark programme of this paper. It is an interpretable Pauli-frame reference baseline, not a claim about the globally best generic Pauli strategy. The point of the paper is instead to diagnose whether a measurement rule that is native to the target topological Hamiltonian remains advantageous after compilation to qubit hardware. This qualifier matters directly for the crossover scale N_c in Eq. (20). Stronger Pauli-side estimators, including shadow-style protocols or more aggressive grouping and ordering heuristics, could shift that

scale by lowering the Pauli-side sampling or measurement overhead [4, 6, 10–12, 35–37]. The present crossover boundaries should therefore be read as conditional on the interpretable PS_{QWC} baseline adopted here rather than as universal thresholds for every Pauli-side strategy.

The same scope applies to the hardware evidence itself. The research work is a descriptive benchmark built from a fixed workload suite, and finite replicate counts; it is not intended as high-power statistical inference about all compilers, all devices, or all Pauli-measurement baselines. Even so, it isolates a broader lesson relevant to topological simulation and topological engineering on qubit-native platforms: if one wants to measure projector- or fusion-based observables more natively, the basis changes must be co-designed with compilation, layout, and noise.

A related scaling point is worth stating explicitly. For the Fibonacci-chain observables studied here, each local fusion-readout basis change is logically a fixed-window primitive built from a constant number of F - and R -move blocks, so the ideal logical size of a single basis-change measurement does not itself grow extensively with n . What grows linearly with system size is the number of local Hamiltonian terms, and hence the number of distinct measurement circuits needed to reconstruct the full estimator. On sparse qubit hardware, routing and placement can then add further size-dependent compiled overhead on top of that local logical structure, so the practical compiled depth can increase more strongly than the ideal anyonic description alone would suggest.

² The count ranges because the logical gates implemented for the Fibonacci chain after being mapped to a sparse heavy-hex coupling graph do not transpile to the same 2Q count.

VII. CONCLUSION

The right benchmark quantity for native measurement in this setting is the fixed-budget mean-squared error of the full energy estimator, not covariance in isolation. On that metric, fusion readout delivers a genuine covariance-driven sampling advantage for Fibonacci-chain workloads and can substantially improve realized performance in noiseless and some hardware regimes. At the same time, the hardware benchmark shows that this advantage does not automatically survive compiled NISQ execution: basis-change overhead and hardware noise can erase or even reverse it.

The practical lesson is broader than this specific model. For topological and projector-dominated problems hosted on qubit-based processors [13, 21–23], the key question is not only whether a native observable basis is physically natural, but whether it remains advantageous after compilation to the host hardware. The present results provide a concrete estimator-level workflow for answering that question.

From a longer-term fault-tolerant perspective, much of this tension is likely to be a NISQ-era effect. Once logical errors are pushed well below the target statistical uncertainty, extra basis-change depth should become more of a resource overhead than an accuracy limiter [16, 38, 39]. That is why the natural next step is not to abandon native readout, but to make it more hardware-aware and to compare it against stronger Pauli estimators on a broader set of devices.

ACKNOWLEDGMENTS

Thanks to colleagues at the Department of Physics at Maynooth University for helpful discussions and feedback during the early stages of this project. I am especially grateful to Joost Slingerland and Jiri Vala for their academic mentorship.

This work was supported in part by Enterprise Ireland through the DTIF programme of the Department of Business, Enterprise, and Innovation under project QCoIr: Quantum Computing in Ireland, A Software Platform for Multiple Qubit Technologies (No. DT 2019 0090B). In addition, I acknowledge the use of IBM Quantum Credits for this work. The views expressed are those of the author and do not reflect the official policy or position of IBM or the IBM Quantum team.

CODE AVAILABILITY

The public code release associated with this work is available as Ref. 40.

Appendix A: Fibonacci anyon background and F/R move conventions

This appendix fixes the minimal conventions needed to interpret the braid-plus-recouple local primitives used throughout the benchmark.

1. Fibonacci F/R data and the induced braid (\mathbf{B} -move) operator

We work with Fibonacci anyons with topological charge set $\{\mathbf{1}, \tau\}$ and fusion rule [25, 26, 28–30, 41]

$$\tau \times \tau = \mathbf{1} + \tau, \quad (\text{A1})$$

with quantum dimension $d_\tau = \varphi$ where $\varphi = (1 + \sqrt{5})/2$ is the golden ratio.

The nontrivial recoupling move is the F move for three τ anyons with total charge τ . In the standard basis where the intermediate fusion channel is $x \in \{\mathbf{1}, \tau\}$, the corresponding 2×2 matrix is

$$F \equiv F_\tau^{\tau\tau\tau} = \begin{pmatrix} \varphi^{-1} & \varphi^{-1/2} \\ \varphi^{-1/2} & -\varphi^{-1} \end{pmatrix}. \quad (\text{A2})$$

Braiding two τ anyons acts diagonally in the direct-fusion basis, with phases determined by the fusion outcome. The corresponding R move can be represented by

$$R \equiv R^{\tau\tau} = \begin{pmatrix} e^{-4\pi i/5} & 0 \\ 0 & e^{3\pi i/5} \end{pmatrix}. \quad (\text{A3})$$

In the fusion-tree basis used for the chain, an elementary braid in the non-direct basis is represented by conjugating the direct-fusion R move into the chosen association of the fusion tree. For the local three-anyon sector this gives the 2×2 braid matrix

$$B \equiv F^\dagger R F. \quad (\text{A4})$$

The many-body operators F_i and B_i in Eq. (3) are the corresponding embeddings of these local primitives into the appropriate windows of the chain.

a. Circuit realization (summary). In our qubit fusion-path encoding, these moves are implemented as small fixed circuits acting on short windows: the R move is a diagonal phase gate in the direct-fusion frame, the F move is the controlled implementation of Eq. (A2), and the braid circuit is the composition

$$U_B = U_F (\mathbb{I} \otimes U_R \otimes \mathbb{I}) U_F^\dagger. \quad (\text{A5})$$

For Fibonacci data the 2×2 recoupling matrix in Eq. (A2) is real, symmetric, and involutory, so U_F^\dagger may be implemented by the same local circuit as U_F . These are the implementation-level identities behind the basis changes $U_i = F_{i+1} B_i$ in Eq. (6) and $U_{\text{BF}}^{(j)} = U_F^{(j+1)} U_B^{(j)}$ in the product-formula expression.

2. Worked example: a braid-plus-recoupling fusion-projector term (BF4)

The simplest local operators in Fibonacci chains are fusion-channel projectors on neighboring anyons. In a fusion-tree basis these are naturally measured in a direct-fusion frame: an F move recouples the fusion tree so that the relevant fusion outcome is represented as a single intermediate label, and the corresponding direct-fusion observable is a diagonal projector, or up to an affine shift a Pauli- Z on the associated encoded qubit.

The BF4 benchmark term is a slightly more involved example in which the physical interaction is most naturally described after braiding and then recoupling into the direct-fusion frame. For a representative prepared state ρ , the operator from Eq. (4) may be read as a next-nearest-neighbor fusion-projector term built from a local braid B_i on the left pair together with the recoupling F_{i+1} that brings the interacting pair into a direct-fusion configuration. In that frame, the observable h_{i+1}^{DF} is simple local projector-like.

For an arbitrary prepared state ρ , the corresponding local energy contribution admits the two equivalent trace forms

$$\langle H_i^{\text{BF4}} \rangle_\rho = \text{Tr} \left(B_i^\dagger F_{i+1}^\dagger h_{i+1}^{\text{DF}} F_{i+1} B_i \rho \right) \quad (\text{A6})$$

$$= \text{Tr} \left(h_{i+1}^{\text{DF}} F_{i+1} B_i \rho B_i^\dagger F_{i+1}^\dagger \right). \quad (\text{A7})$$

These two forms make the measurement logic transparent. In PS_{QWC} , one measures a grouped Pauli decomposition of the mapped operator content entering Eq. (4). In FR, one instead appends the basis change $U_i = F_{i+1} B_i$ to the state-preparation circuit and measures the simple direct-fusion observable h_{i+1}^{DF} directly. This local worked example is the basic reason that fusion readout is physically natural for the Hamiltonian terms studied in the main text.

Appendix B: Selected Crossover Scaling Grids

Figures 5 and 6 collect the fitted empirical-MSE scaling plots for the selected hardware cells discussed in the crossover analysis. For the digital benchmark we show plots for the shallow, intermediate, and deep Trotter steps $s = 1, 3, 6$ across qubit counts $n = 5, 7, 9, 11$. For the optimized-state VQE hardware benchmark, we show the analogous fits at $n = 5, 7, 9, 11$. In every panel the empirical MSE data are indicated with point markers, while the least-squares fits of the form $\alpha_m + \beta_m/N$ are indicated with both solid lines (for FR) and dashed-solid lines (for PS_{QWC}), and the dashed vertical guide marks the fitted positive-budget crossing when it lies inside the sampled window. Panels whose fitted crossing lies below or above the sampled range are labeled accordingly, as well as panels with no positive fitted crossing.

Appendix C: Paired Measurement-Count Correlations

To characterize how compiled measurement overhead correlates with realized estimator performance, we analyze paired FR-minus-PS observables within each hardware cell. For a fixed workload, the state-preparation circuit is common to both measurement schemes, so the FR-minus-PS count difference removes the shared state-preparation contribution and isolates the method-dependent compiled measurement layer. We then correlate this paired count observable with the corresponding paired error observable while conditioning on the workload parameter that sets the dominant background scale: Trotter step s in the digital Floquet benchmark and total shot budget N in the locked-state VQE benchmark.

Figure 7 resolves the digital hardware data into three fixed-step panels, $s = 1, 3, 6$. Within each panel, every point is a fixed (n, N) hardware cell and the ordinate is the instantaneous error-ratio observable $\log_{10}(\text{MSE}_{\text{FR}}/\text{MSE}_{\text{PS}})$ at that budget. The panelwise correlations are obtained after conditioning on shot budget, so each reported r measures how the FR-minus-PS compiled measurement count varies with the FR-to-PS error ratio across qubit size at fixed N . For the total compiled measurement count (1Q+2Q), the resulting correlations are weak and step dependent: $r = +0.14$ at $s = 1$, $r = -0.45$ at $s = 3$, and $r = -0.29$ at $s = 6$. Since negative values of the log-ratio correspond to FR-favorable performance, those 3-panel plots show that FR become more favorable with increased circuit depth at higher Trotter step value.

Figure 8 applies the same vertical observable to the locked-state VQE hardware data. Here each point is again a fixed (n, N) cell, and the budget-conditioned correlation between the FR-minus-PS total compiled measurement count and $\log_{10}(\text{MSE}_{\text{FR}}/\text{MSE}_{\text{PS}})$ is positive, $r = +0.46$. The positive sign means that a larger compiled FR measurement layer tends to coincide with a larger PS-QWC-favorable error ratio, consistent with the shallow locked-state circuits leaving the method-dependent measurement block comparatively exposed.

The correlation structure therefore differs between the two hardware workloads. In the digital Floquet benchmark, the relation between compiled measurement-count difference and the FR/PS error ratio is weak but leans more to be negative at larger Trotter steps, indicating a weak correlation between the large FR measurement circuits and the observed error. In the locked-state VQE benchmark, the same paired observable is positively correlated with the error ratio on the common log-scale, indicating that compiled measurement overhead is a more relevant control parameter in the shallow-circuit regime.

Beyond the gate-count diagnostic itself, other plausible contributors to the hardware reversal include layout-sensitive routing on the heavy-hex graph, and the nonuniform assignment-error landscape across candidate qubits.

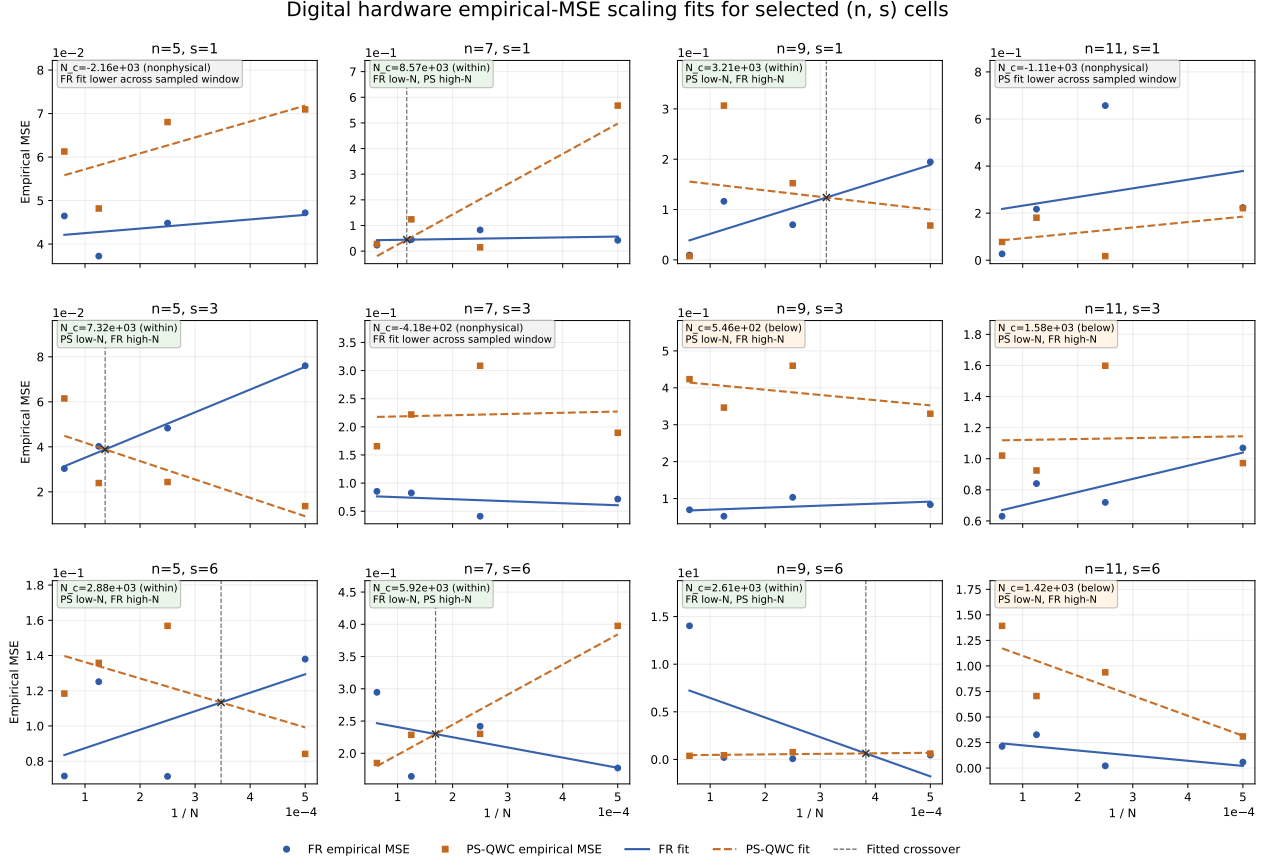


FIG. 5. Digital hardware empirical-MSE scaling fits for the selected cells $(n, s) \in \{5, 7, 9, 11\} \times \{1, 3, 6\}$. The point markers show the empirical MSE values for FR and PS_{QWC}, while the solid and dashed lines show the fitted laws $\alpha_m + \beta_m/N$, and dashed vertical lines mark fit positive-budget crossings that fall inside the sampled budget window. Panel annotations report the fitted crossing budget when it exists and indicate whether it lies below, within, or above the sampled range.

Appendix D: Hardware Transpilation Methodology

The hardware benchmark is descriptive rather than inferential due to the current prohibitive cost of running experiments on quantum hardware, but the compilation context still matters because the central question of the paper is whether the additional basis-change depth required by native readout survives under current-device constraints. Table III collects the configuration of the hardware.

That compiled-hardware perspective is also the one now relevant to recent processor-level demonstrations of non-Abelian braiding and topological-order engineering, where native logical observables must still be accessed through the compilation and noise profile of the host platform [21–23]. All logical-circuit construction, transpilation, and execution were carried out in a Qiskit-based workflow [42].

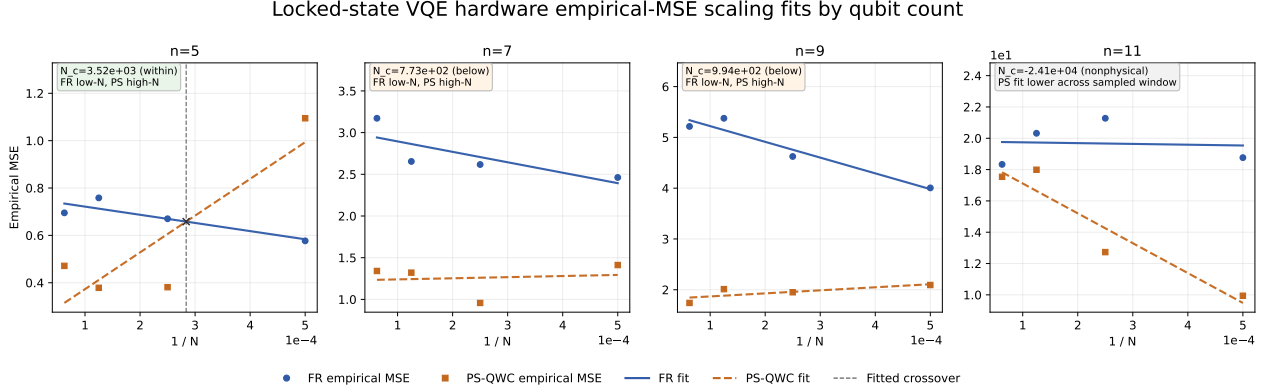


FIG. 6. Optimized-state VQE hardware empirical-MSE scaling fits for qubit counts $n = 5, 7, 9, 11$. Point markers show the empirical MSE values for FR and PS_{QWC} , while solid and dashed lines show the fitted laws $\alpha_m + \beta_m/N$, and dashed vertical lines mark fit positive-budget crossings that fall inside the sampled budget window. The VQE panels make clear that most fitted crossings for this workload already sit below the sampled budget range, consistent with the small fitted N_c values reported in the main text.

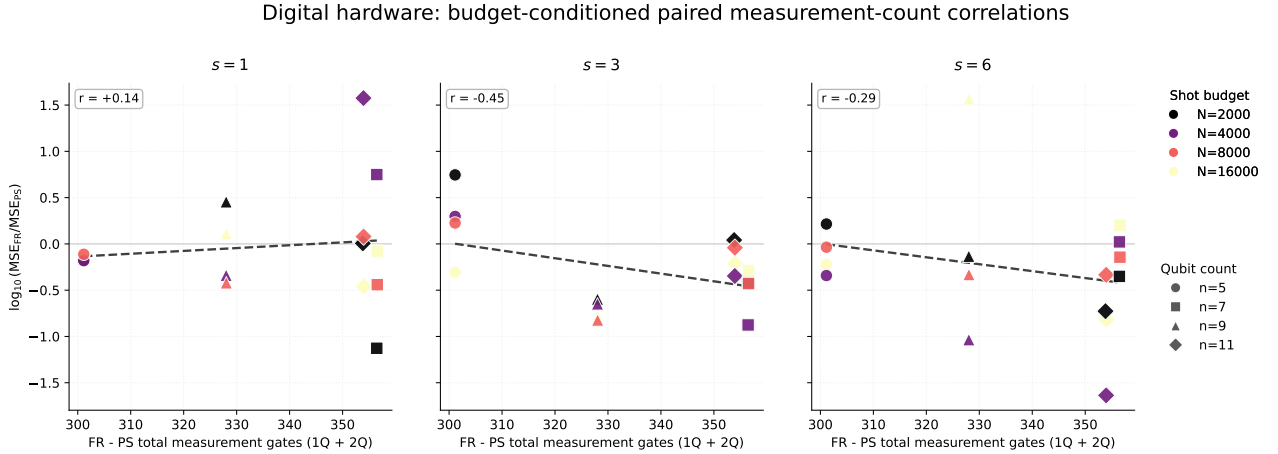


FIG. 7. Digital paired measurement-count correlations for the hardware Floquet benchmark. The three panels correspond to fixed Trotter steps $s = 1, 3, 6$. Within each panel, each point is one fixed (n, N) hardware cell. The horizontal axis is the FR-minus-PS total compiled measurement-gate count $(1Q+2Q)$, and the vertical axis is $\log_{10}(\text{MSE}_{\text{FR}}/\text{MSE}_{\text{PS}})$ at the corresponding budget. Point color denotes shot budget, marker shape denotes qubit count, the dashed line is the budget-conditioned least-squares trend guide, and the inset reports the panelwise correlation coefficient r .

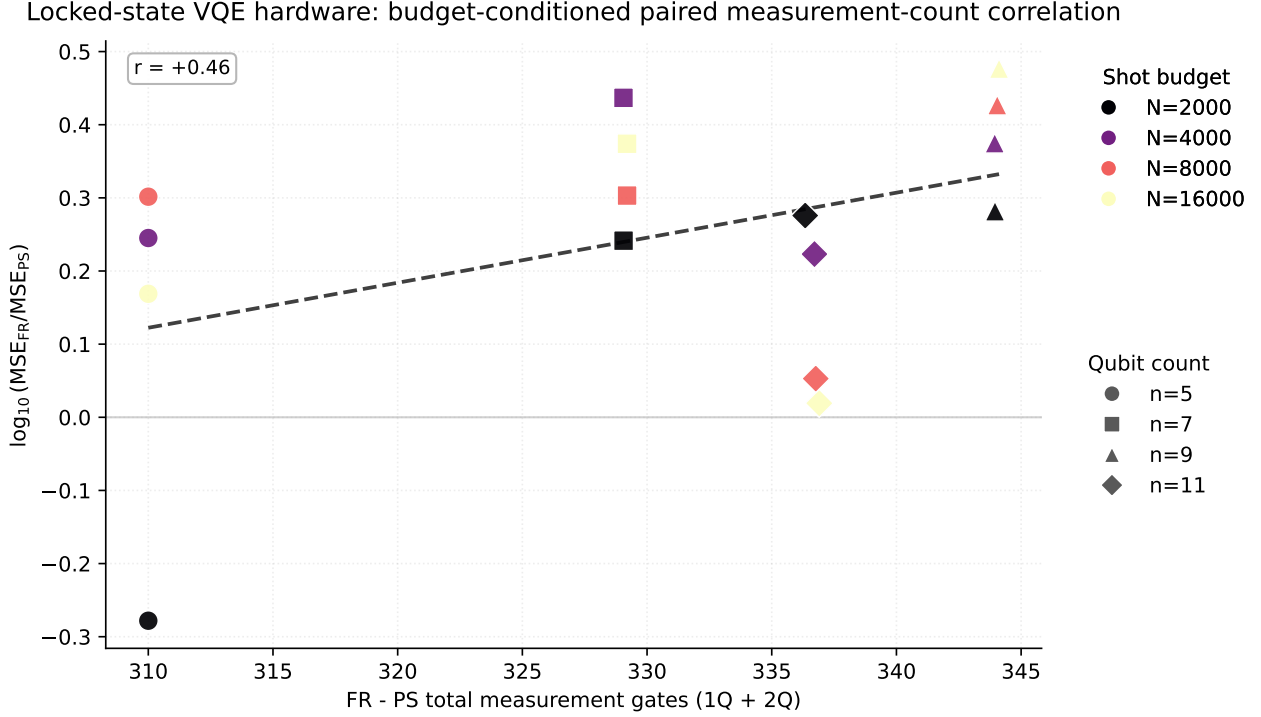


FIG. 8. Locked-state VQE paired measurement-count correlation for the hardware benchmark. Each point is one fixed (n, N) hardware cell. The horizontal axis is the FR-minus-PS total compiled measurement-gate count (1Q+2Q), and the vertical axis is $\log_{10}(\text{MSE}_{\text{FR}}/\text{MSE}_{\text{PS}})$ at that budget. Point color denotes shot budget, marker shape denotes qubit count, the dashed line is the budget-conditioned least-squares trend guide, and the inset reports the correlation coefficient r .

TABLE III. Hardware-methodology details for the benchmark. The upper panel lists the `ibm_pittsburgh` calibration. The lower panel reports the matched-budget measurement allocations and endpoint transpiled circuit-resource ranges for representative digital and optimized-state VQE workloads.

Backend quantity	Value
Backend and calibration date	<code>ibm_pittsburgh</code> , calibration record 2026-05-04 12:56 UTC
Execution mode	IBM Quantum hardware campaign on <code>ibm_pittsburgh</code> ; queue delay is not part of the estimator analysis
Backend size	156 qubits, 352 directed couplers
Basis gates	<code>cz, id, rx, rz, rzz, sx, x</code>
Transpilation and mitigation	Qiskit preset pass manager, optimization level 1; no readout mitigation, dynamical decoupling, or resilience-level post-processing
Readout assignment error	Mean 0.76%, range 0.15%–13.27% across qubits
Native two-qubit calibration	<code>cz</code> gate; mean error 0.58%, median 0.145%, range 0.077%–13.72% across calibrated couplers
Excluded coupler note	10 couplers reported placeholder <code>gate_error=1.0</code> entries in the backend calibration record and were excluded from the quoted <code>cz</code> mean.

Endpoint	FR allocation at $B = 2000$	PS-QWC allocation at $B = 2000$	FR depth	FR 2Q	PS depth	PS 2Q
Digital $n = 5, s = 1$	5 observables, 400 each	15 groups, 133–134 each	2444–2711	1073–1200	2330–2363	1029–1053
Digital $n = 11, s = 6$	17 observables, 117–118 each	22 groups, 90–91 each	30262–33745	21779–22125	30137–34553	21834–22059
VQE $n = 5, d = 3$	5 observables, 400 each	15 groups, 133–134 each	189–469	98–222	84–94	51–54
VQE $n = 11, d = 4$	17 observables, 117–118 each	22 groups, 90–91 each	223–523	240–370	127–188	190–193

-
- [1] J. Preskill, Quantum computing in the nisq era and beyond, *Quantum* **2**, 79 (2018).
- [2] A. Peruzzo, J. McClean, P. Shadbolt, M.-H. Yung, X.-Q. Zhou, P. J. Love, A. Aspuru-Guzik, and J. L. O'Brien, A variational eigenvalue solver on a photonic quantum processor, *Nature communications* **5**, 4213 (2014).
- [3] J. R. McClean, J. Romero, R. Babbush, and A. Aspuru-Guzik, The theory of variational hybrid quantum-classical algorithms, *New Journal of Physics* **18**, 023023 (2016).
- [4] V. Verteletskyi, T.-C. Yen, and A. F. Izmaylov, Measurement optimization in the variational quantum eigensolver using a minimum clique cover, *Journal of Chemical Theory and Computation* **16**, 240 (2020).
- [5] P. Gokhale *et al.*, Minimizing state preparations in variational quantum eigensolver by partitioning into commuting families, arXiv preprint arXiv:1907.13623 (2019), arXiv:1907.13623.
- [6] P. Gokhale, O. Angiuli, Y. Ding, K. Gui, T. Tomesh, M. Suchara, M. Martonosi, and F. T. Chong, Optimization of simultaneous measurement for variational quantum eigensolver applications, in *2020 IEEE International Conference on Quantum Computing and Engineering (QCE)* (IEEE, 2020) pp. 379–390.
- [7] A. F. Izmaylov, T.-C. Yen, and I. G. Ryabinkin, Revising the measurement process in the variational quantum eigensolver: Is it possible to reduce the number of terms in a molecular hamiltonian?, *Chemical Science* **10**, 3746 (2019).
- [8] J. M. Kübler, A. Arrasmith, L. Cincio, and P. J. Coles, An adaptive optimizer for measurement-frugal variational algorithms, *Quantum* **4**, 263 (2020).
- [9] A. Gu, A. Lowe, P. A. Dub, P. J. Coles, and A. Arrasmith, Adaptive shot allocation for fast convergence in variational quantum algorithms, arXiv preprint arXiv:2108.10434 10.48550/arXiv.2108.10434 (2021).
- [10] W. J. Huggins, J. R. McClean, N. C. Rubin, Z. Jiang, N. Wiebe, K. B. Whaley, and R. Babbush, Efficient and noise resilient measurements for quantum chemistry on near-term quantum computers, *npj Quantum Information* **7**, 23 (2021).
- [11] H.-Y. Huang, R. Kueng, and J. Preskill, Predicting many properties of a quantum system from very few measurements, *Nature Physics* **16**, 1050 (2020).
- [12] T.-C. Yen and A. F. Izmaylov, Exhaustive search for commuting groups of pauli observables in variational quantum eigensolvers, *Journal of Chemical Theory and Computation* **19**, 1184 (2023).
- [13] M. A. Levin and X.-G. Wen, String-net condensation: A physical mechanism for topological phases, *Physical Review B* **71**, 045110 (2005).
- [14] D. Gottesman, An introduction to quantum error correction, in *Quantum Computation*, Proceedings of Symposia in Applied Mathematics, Vol. 58 (American Mathematical Society, 2002) pp. 221–235.
- [15] E. Dennis, A. Kitaev, A. Landahl, and J. Preskill, Topological quantum memory, *Journal of Mathematical Physics* **43**, 4452 (2002).
- [16] A. G. Fowler, M. Mariantoni, J. M. Martinis, and A. N. Cleland, Surface codes: Towards practical large-scale quantum computation, *Physical Review A* **86**, 032324 (2012).
- [17] H. Bombin, Topological order with a twist: Ising anyons from an abelian model, *Physical Review Letters* **105**, 030403 (2010).
- [18] B. J. Brown, K. Laubscher, M. S. Kesselring, and J. R. Wootton, Poking holes and cutting corners to achieve clifford gates with the surface code, *Physical Review X* **7**, 021029 (2017).
- [19] H. Bernien, S. Schwartz, A. Keesling, H. Levine, A. Omran, H. Pichler, S. Choi, A. S. Zibrov, M. Endres, M. Greiner, V. Vuletić, and M. D. Lukin, Probing many-body dynamics on a 51-atom quantum simulator, *Nature* **551**, 579 (2017).
- [20] A. Browaeys and T. Lahaye, Many-body physics with individually controlled rydberg atoms, *Nature Physics* **16**, 132 (2020).
- [21] Google Quantum AI *et al.*, Non-Abelian braiding of graph vertices in a superconducting processor, *Nature* **618**, 264 (2023).
- [22] M. Iqbal, N. Tantivasadakarn, R. Verresen, *et al.*, Non-Abelian topological order and anyons on a trapped-ion processor, *Nature* **626**, 505 (2024).
- [23] S. Xu *et al.*, Non-Abelian braiding of fibonacci anyons with a superconducting quantum processor, *Nature Physics* **20**, 1116 (2024).
- [24] B. Field and T. Simula, Introduction to topological quantum computation with non-abelian anyons, *Quantum Science and Technology* **3**, 045004 (2018).
- [25] C. Nayak, S. H. Simon, A. Stern, M. Freedman, and S. Das Sarma, Non-abelian anyons and topological quantum computation, *Reviews of Modern Physics* **80**, 1083 (2008).
- [26] J. K. Pachos, *Introduction to topological quantum computation* (Cambridge University Press, 2012).
- [27] R. N. Pfeifer and S. Singh, Finite density matrix renormalization group algorithm for anyonic systems, *Physical Review B* **92**, 115135 (2015).
- [28] S. Singh, R. N. Pfeifer, G. Vidal, and G. K. Brennen, Matrix product states for anyonic systems and efficient simulation of dynamics, *Physical Review B* **89**, 075112 (2014).
- [29] B. M. Ayeni, S. Singh, R. N. Pfeifer, and G. K. Brennen, Simulation of braiding anyons using matrix product states, *Physical Review B* **93**, 165128 (2016).
- [30] N. Kirchner, D. Millar, B. M. Ayeni, A. Smith, J. K. Slingerland, and F. Pollmann, Numerical simulation of non-abelian anyons, *Physical Review B* **107**, 195129 (2023).
- [31] B. M. Ayeni, R. N. C. Pfeifer, and G. K. Brennen, Phase transitions on a ladder of braided non-abelian anyons, *Phys. Rev. B* **98**, 045432 (2018).
- [32] A. Kandala, A. Mezzacapo, K. Temme, M. Takita, M. Brink, J. M. Chow, and J. M. Gambetta, Hardware-efficient variational quantum eigensolver for small molecules and quantum magnets, *Nature* **549**, 242 (2017).
- [33] B. M. Ayeni, Efficient particle-conserving symmetric quantum circuits, *Phys. Rev. A* **111**, 022629 (2025).
- [34] X. Bonet-Monroig, R. Babbush, T. E. O'Brien, and C. Ryan-Anderson, Low-cost error mitigation by symmetry verification, *Physical Review X* **10**, 031064 (2020).

- [35] S. Hadfield *et al.*, Measurements of quantum hamiltonians with locally-biased classical shadows, *Communications in Mathematical Physics* **391**, 951 (2022).
- [36] O. Crawford, B. van Straaten, D. Wang, Z. Parks, E. T. Campbell, and S. Brierley, Efficient quantum measurement of pauli operators in the presence of finite sampling error, *Quantum* **5**, 385 (2021).
- [37] A. Zhao *et al.*, Measurement reduction in variational quantum algorithms, *Physical Review A* **104**, 032406 (2021).
- [38] E. T. Campbell, B. M. Terhal, and C. Vuillot, Roads towards fault-tolerant universal quantum computation, *Nature* **549**, 172 (2017).
- [39] D. Litinski, A game of surface codes: Large-scale quantum computing with lattice surgery, *Quantum* **3**, 128 (2019).
- [40] B. M. Ayeni, Native topological readout benchmark research source code, <https://github.com/TeeAyeni/qwc-hamiltonian-benchmark-workflows> (2026), gitHub repository, version 1.0.0.
- [41] R. N. Pfeifer, P. Corboz, O. Buerschaper, M. Aguado, M. Troyer, and G. Vidal, Simulation of anyons with tensor network algorithms, *Physical Review B* **82**, 115126 (2010).
- [42] Qiskit contributors, Qiskit: An open-source framework for quantum computing (2023).